

Prediction of single cell mechanical properties in microchannels based on deep learning*

Jiajie GONG¹, Xinyue LIU^{1,2}, Yancong ZHANG¹, Fengping ZHU^{3,†}, Guohui HU^{1,†}

1. Shanghai Institute of Applied Mathematics and Mechanics, School of Mechanics and Engineering Science, Shanghai Frontier Science Center of Mechatronics, Shanghai Key Laboratory of Mechanics in Energy Engineering, Shanghai University, Shanghai 200072, China;
2. Shanghai Institute of Aircraft Mechanics and Control, Shanghai 200092, China;
3. Department of Neurosurgery, Huashan Hospital, Shanghai Medical College, Fudan University, Shanghai 200040, China

(Received May 5, 2024 / Revised Sept. 23, 2024)

Abstract Traditional methods for measuring single-cell mechanical characteristics face several challenges, including lengthy measurement times, low throughput, and a requirement for advanced technical skills. To overcome these challenges, a novel machine learning (ML) approach is implemented based on the convolutional neural networks (CNNs), aiming at predicting cells' elastic modulus and constitutive equations from their deformations while passing through micro-constriction channels. In the present study, the computational fluid dynamics technology is used to generate a dataset within the range of the cell elastic modulus, incorporating three widely-used constitutive models that characterize the cellular mechanical behavior, i.e., the Mooney-Rivlin (M-R), Neo-Hookean (N-H), and Kelvin-Voigt (K-V) models. Utilizing this dataset, a multi-input convolutional neural network (MI-CNN) algorithm is developed by incorporating cellular deformation data as well as the time and positional information. This approach accurately predicts the cell elastic modulus, with a coefficient of determination R^2 of 0.999, a root mean square error of 0.218, and a mean absolute percentage error of 1.089%. The model consistently achieves high-precision predictions of the cellular elastic modulus with a maximum R^2 of 0.99, even when the stochastic noise is added to the simulated data. One significant feature of the present model is that it has the ability to effectively classify the three types of constitutive equations we applied. The model accurately and reliably predicts single-cell mechanical properties, showcasing a robust ability to generalize. We demonstrate that incorporating deformation features at multiple time points can enhance the algorithm's accuracy and generalization. This algorithm presents a possibility for high-throughput, highly automated, real-time, and precise characterization of single-cell mechanical properties.

* Citation: GONG, J. J., LIU, X. Y., ZHANG, Y. C., ZHU, F. P., and HU, G. H. Prediction of single cell mechanical properties in microchannels based on deep learning. *Applied Mathematics and Mechanics (English Edition)*, **45**(11), 1857–1874 (2024) <https://doi.org/10.1007/s10483-024-3187-6>

† Corresponding authors, E-mails: ghhu@staff.shu.edu.cn, fpzhu@fudan.edu.cn

Project supported by the National Natural Science Foundation of China (Nos. 12332016, 12172209, and 12202258) and the Shanghai Gaofeng Project for University Academic Program Development

©The Author(s) 2024

Key words cell deformation, single-cell mechanics, machine learning (ML), constitutive law, convolutional neural network (CNN)

Chinese Library Classification O368

2010 Mathematics Subject Classification 76D05, 76Z99

1 Introduction

Cells represent the fundamental units of living organisms. Gaining profound insights into their operational mechanisms and functional attributes constitutes one of the principal objectives of biological research. Cellular mechanical characteristics are predominantly determined by the material properties, structures, and interactions among the cell's components, i.e., the cytoskeleton, cell membrane, nucleus, and organelles^[1–2]. To date, numerous diseases and biological processes are associated with alterations in cellular mechanical properties, including the increased deformation capacity of invasive cancer cells^[3], and the changes in deformability during stem cell differentiation^[4–6]. Consequently, cellular mechanical properties have emerged as biomarkers indicative of various diseases and cellular state transitions^[7–9], with the elastic modulus serving as a critical phenotypic marker capable of revealing cellular adaptability, differentiation, and pathological changes^[10–12]. Furthermore, understanding cellular mechanics carries substantial significance in cell therapy. For example, precisely measuring cell elasticity enables us to regulate the degree of pore formation in the cell membranes induced by applied force, thereby facilitating effective control over transmembrane substance transport^[13–14]. Thus, the investigation of cellular mechanical properties holds potential significance across the domains of cellular biology and clinical medicine.

The rapid and accurate measurement of cellular mechanical properties is a prerequisite for their practical application. Due to the factors such as micrometer size and heterogeneity^[15], the quantification of cells' mechanical attributes presents profound challenges. In recent years, researchers have utilized principles from engineering physics, microfluidics, and microelectromechanical systems to develop precise methodologies for measuring cellular mechanical properties at the single-cell level, e.g., atomic force microscopy (AFM), micropipette aspiration, parallel plate technique, magnetic tweezers, optical stretcher, optical tweezers, acoustic methods, particle-tracking micro-rheology, and integrated multifaceted measurement approaches^[16–17]. These techniques are generally operated by applying direct or non-contact forces to the whole cell or specific regions, causing deformation and geometric changes, which are then fitted to theoretical prediction, and inversely infer cellular mechanical properties. However, the throughput of these methods is typically limited to 10–100 cells per hour^[18], making the high-throughput characterization of biological samples challenging.

The investigation of cellular mechanics requires high-throughput data due to cell diversity. A large dataset is essential for accurately representing the mechanical properties and features of a cell population, ensuring statistical reliability. High-throughput measurements are crucial in clinical scenarios, enabling rapid screening and monitoring of numerous cells in samples ranging from thousands to millions. This minimizes potential physical changes during the measurements that could affect accuracy and significantly boost efficiency, allowing for early patient treatment. Therefore, there is a pressing need for cellular mechanical property measurement techniques to be highly efficient and capable of high-throughput analyses.

Microfluidic methods have the potential to overcome the limitation of low throughput, achieving throughputs of up to 10^3 – 10^4 cells per second in experiments. However, the complexity of forces exerted on cells in microfluidic environment compromises the precision of this technology. Therefore, it is commonly employed to classify cells according to their types and pathological changes based on the deformation patterns exhibited by a large number of cells within microfluidic devices^[19–20]. Broadly, there are mainly three microfluidic approaches to measure cell deformability, i.e., micro-constrictions^[21–23], extensional flow^[24–26], and shear flow^[27–28].

Among these, micro-constriction can further be categorized into contact-based (where the cell size exceeds the constriction dimension) and contactless (where the cell size is smaller than the constriction dimension). In the present study, we employ a contactless micro-constriction measurement method, which not only offers the advantage of simple and easily fabricated microfluidic chips, but also minimizes the cell damage caused by excessive deformation and avoids channel clogging. Moreover, the microfluidic technology can be integrated with real-time optical monitoring, achieving real-time deformability cytometry (RT-DC) and real-time fluorescence and deformability cytometry (RT-FDC)^[29–30]. Real-time deformation techniques enable immediate image acquisition and analysis, allowing for label-free screening of heterogeneous cell samples without significant size limitations, and identifying subpopulations based on mechanical properties. Additionally, by assessing the deformation in single snapshots of each cell, material properties such as Young's modulus can be deduced^[31–32].

High throughput in microfluidics can rapidly generate a large amount of raw data, aligning with the prevalent big data processing tools, i.e., machine learning (ML). The essential idea of ML involves utilizing algorithms and mathematical models to analyze vast datasets, extracting useful information and structures to infer nonlinear relationships between the data and its corresponding measurements. These algorithms and models can be adjusted and optimized based on the features of the data and the requirements of the target task. Integrating ML data processing with RT-DC/RT-FDC methods can provide a versatile tool applicable for real-time applications^[33]. ML methods have found numerous applications in the biomedical and mechanical fields, including cell classification^[34–36], morphological analysis of cells^[37–38], disease diagnosis^[39–42], and blood flow reconstruction^[43]. In the mechanical characterization of capsules, Lin et al.^[44] proposed a prediction method based on a deep convolutional neural network (DCNN). This method can identify the constitutive equation of microcapsule membranes from deformed cell images in a steady flow through a tube and estimate related parameters. Lin et al.^[45] considered deformation images of cells at multiple time moments, in which the neural network (NN) consists of a DCNN connected to a long short-term memory (LSTM) network. As a result, they achieved mean absolute percentage errors (R_{MAPE}) as low as 3.65% and 3.42% for the predicted capillary number and membrane viscosity, respectively. In addition to image processing, Guo et al.^[46] proposed a multilayer perceptron (MLP) method that directly treats the contours of a stable-state capsule. They found that the regression mean absolute percentage errors for the two capillary numbers are 4.2% and 7.6%, respectively, which, although slightly larger than the DCNN-LSTM method, significantly reduced prediction delay. However, this network does not effectively distinguish between the Skalak (SK) model and Hooke's model. Nguyen et al.^[47] simulated the deformation of capsules in micro-constriction channels based on the fluid-structure interaction (FSI) method. They successfully predicted capsule stiffness by training a convolutional neural network (CNN) on deformed cell images and three-dimensional (3D) surface data points. ML methods have been also used to characterize the mechanics of tissues. Liang et al.^[48] predicted the elastic properties of collagen tissue using a CNN. Martínez-Martínez et al.^[49] used decision trees, extremely randomized trees, and random forests for real-time deformation prediction of breast tissue. Xiao et al.^[50] used a deep learning model based on dual energy X-ray absorptiometry images to predict the apparent stiffness tensor of bone trabecular cubes with high fidelity.

This study aims at precisely predicting the constitutive relationship of biological cells based on their deformations in contactless micro-constriction channels. Contactless micro-constriction channels are microfluidic techniques employed for high-throughput cell deformation experiments, wherein cells with varying mechanical properties exhibit distinct deformations when passing through variable section microchannels. NNs, by learning the complex relationship between cellular deformations and mechanical properties, can estimate their constitutive equations and associated parameters. In the present study, numerical simulations of cell deformations within microchannels are conducted utilizing the COMSOL Multiphysics software. The

database generated from these simulations provides detailed information about cell shapes with different mechanical properties at various time moments, the relevant constitutive equations, and the positional data. Utilizing this dataset, we develop a novel multi-input convolutional neural network (MI-CNN) prediction algorithm to characterize the deformation features of cells by leveraging spatiotemporal information from cell contours across a time series. The algorithm can associate the database with the corresponding elastic modulus E (regression problem), and concurrently identify the type of constitutive equations governing the cell's behavior (classification problem). To mimic experimental scenarios in reality, random noise is incorporated into the dataset to test the robustness of the present model.

2 Finite element simulations

2.1 Problem formulation

An axisymmetric microchannel model is adopted in this study. Although a 3D asymmetric geometry is closer to reality, the axisymmetric model is more straightforward and easier to implement in engineering applications, making it suitable for practical deep learning prediction. This is because the training dataset needs to be expanded by incorporating asymmetric deformations, requiring more cameras to record 3D deformation of cells, which inevitably increases the complexity and cost of the measuring device. Furthermore, the NN architecture needs to be adjusted by increasing the degrees of freedom to accurately capture the features of asymmetric deformations. Regularization and hyperparameter optimization may be necessary to improve the model's generalization ability and robustness, which also reduce the efficiency of the prediction.

Figure 1 illustrates the axisymmetric geometry and dimensions of the microchannel in simulations, where the diameter of the inlet is $30\text{ }\mu\text{m}$, and the length of the channel is $170\text{ }\mu\text{m}$. The diameter and length of the constriction of the micro-constriction are $20\text{ }\mu\text{m}$ and $100\text{ }\mu\text{m}$, respectively. Cells are represented by circles with a diameter D of $12\text{ }\mu\text{m}$, and the thickness of the cell membrane is $0.15\text{ }\mu\text{m}$. The cells are located at the center of the microchannel initially. When the suspended cells translate under the pressure gradient, the flows in the channel with a variable section result in non-uniform velocity distribution and velocity gradient, as well as deformation in cell membranes due to shear forces. We assume that both the intracellular and extracellular fluids are incompressible Newtonian fluids, with the same density ρ_f and viscosity μ , which are given as $\rho_f = 1\,000\text{ kg}\cdot\text{mm}^{-3}$ and $\mu = 0.001\text{ Pa}\cdot\text{s}$, respectively. The pressure drop ΔP between the inlet and outlet of the system is set to be 25 Pa .

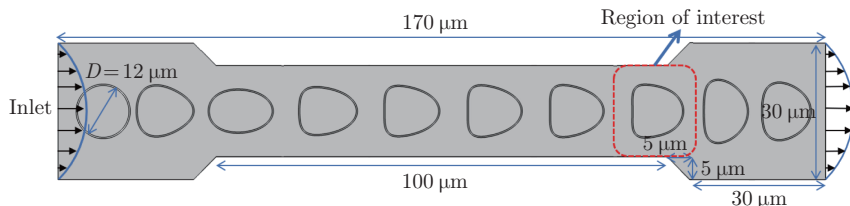


Fig. 1 Schematic diagram of the numerical simulation model (color online)

The numerical simulations are conducted using the COMSOL Multiphysics software. The arbitrary Lagrangian-Eulerian (ALE) description method is employed to simulate the FSI problems^[51]. The advantage of this method lies in its ability to establish corresponding governing equations in the moving coordinate system, effectively addressing the challenges associated with large deformation in FSI.

In the moving ALE coordinate system, the relationship between the time derivative of matter

and the time derivative of the reference system is

$$\frac{\partial f(\mathbf{X}, t)}{\partial t} = \frac{\partial f(\mathbf{x}, t)}{\partial t} + (\mathbf{u} - \mathbf{v}) \frac{\partial f(\chi, t)}{\partial t}, \quad (1)$$

where \mathbf{X} is the coordinate in the Lagrangian coordinate system, \mathbf{x} is the coordinate in the Eulerian coordinate system, χ is the coordinate in the ALE coordinate system, \mathbf{u} is the velocity of moving particles, and \mathbf{v} is the speed of motion in the reference frame in ALE.

The FSI module is used to simulate the coupling flow around the cells^[52], which involves the governing equations for fluids, solids, and FSI boundary conditions. Considering the moving grids, non-dimensional Navier-Stokes equations are written as^[53–54]

$$\nabla \cdot \mathbf{u} = 0, \quad (2)$$

$$\rho_f \left(\frac{\partial \mathbf{u}}{\partial t} + (\mathbf{v} - \mathbf{w}) \cdot \nabla \mathbf{v} \right) - \nabla \cdot \boldsymbol{\sigma}^F = 0, \quad (3)$$

where ρ_f is the fluid density, \mathbf{v} is the fluid velocity, \mathbf{w} is the grid velocity, $\mathbf{v} - \mathbf{w}$ is the relative velocity, and $\boldsymbol{\sigma}^F$ is the fluid stress tensor. The fluid stress tensor $\boldsymbol{\sigma}^F$ is^[55]

$$\boldsymbol{\sigma}^F = -p\mathbf{I} + \mu(\nabla\mathbf{u} + (\nabla\mathbf{u})^T) = -p\mathbf{I} + \mu\nabla^2\mathbf{u}, \quad (4)$$

where $-p\mathbf{I}$ is the fluid pressure, \mathbf{I} is the unit diagonal matrix, and μ is the fluid dynamic viscosity. The negative sign indicates that the force is directed from the pressure from high to low values.

The structural deformations are solved using an elastic formulation and a nonlinear geometry formulation to allow large deformations. Assume that the cell is isotropic. Then, when the cell moves in a micro-constriction channel, the cell boundary will undergo corresponding deformation due to the applied load from the surrounding fluid, which is given by

$$\rho_s \frac{\partial^2 \mathbf{d}}{\partial t^2} - \boldsymbol{\sigma}^S = 0, \quad (5)$$

where ρ_s is the solid density, \mathbf{d} is the displacement of nodes and it includes the displacements in two directions $\mathbf{d} = \{d_x, d_y\}^T$, and $\boldsymbol{\sigma}^S$ is the Cauchy stress.

The interaction between the solid and the fluid at the contact boundary implies that, at the coupled interface, the velocities and stresses of the fluid and the solid should be equal in magnitude and opposite in direction^[56], which yields

$$\boldsymbol{\sigma}_s \cdot \mathbf{n} = \boldsymbol{\sigma}_f \cdot \mathbf{n}, \quad \mathbf{u}_f = \mathbf{u}_s = \mathbf{w}, \quad (6)$$

where $\boldsymbol{\sigma}_s$ is the stress on solids, $\boldsymbol{\sigma}_f$ is the stress on fluids, \mathbf{u}_s is the velocity of the solid boundary, \mathbf{u}_f is the velocity of the fluid boundary, and \mathbf{n} is the boundary normal vector.

2.2 Constitutive laws of cells

To study the translocation of cells in the micro-constriction, the cell deformation depends not only on the cell's stiffness but also on the fluid velocity, the relative size of the cell, and the internal structure of the cell. In our database, for the sake of simplification, the pressure difference ΔP , cell size, and microchannel dimensions remain fixed, so the influence of fluid velocity and relative cell size on deformation is not considered here.

The stiffness of the cell primarily depends on its constitutive equation and corresponding parameters. There are various constitutive equations commonly used for describing cells, which are mainly categorized into continuous theoretical models ignoring cell structure and microstructure models based on cell structure and function^[57]. Since we try to calculate a large amount of data through numerical simulations, the continuous theoretical models are considered, treating the cell membrane as an elastic shell structure and the interior and exterior of the cell as a

viscous liquid. Therefore, the influence of the internal structure of the cell on deformation is neglected. The constitutive equations that describe this shell-like cell model mainly include the Mooney-Rivlin (M-R) model^[21,26,57], strain-softening Neo-Hookean (N-H) model^[57], viscoelastic Kelvin-Voigt (K-V) model^[58], strain-hardening SK model, and Evans & Skalak model^[59]. The current database includes data for the M-R, N-H, and K-V material models, and future work will involve calculating data for various constitutive equations, to expand the database and enhance the model's ability in generalization.

The M-R model is a widely adopted material constitutive equation for describing the stress-strain relationship of elastic materials, particularly for nonlinear behavior under large strains. The strain energy density function associated with the M-R model is written as^[21,26]

$$W^{\text{MR}} = c_1(J_1 - 3) + c_2(J_2 - 3) + \frac{\kappa}{2}(J_3 - 1)^2, \quad (7)$$

where c_1 and c_2 are material constants, and κ denotes the bulk modulus. For thin elastic shell materials, the relationship for the elastic modulus is given by $E = 6(c_1 + c_2)$ ^[59-61], with detailed derivations provided in Appendix S1 in the electronic supplementary material (see <https://doi.org/10.1007/s10483-024-3187-6>). J_1 , J_2 , and J_3 are invariants related to the deformation gradient \mathbf{F} , I_1 , I_2 , and I_3 are strain invariants, and

$$\begin{cases} J_1 = I_1 I_3^{-\frac{1}{3}}, & J_2 = I_2 I_3^{-\frac{2}{3}}, & J_3 = I_3^{\frac{1}{2}}, \\ I_1 = C_{kk}, & I_2 = \frac{1}{2}(I_1^2 - C_{ij}C_{ij}), & I_3 = \det(\mathbf{C}). \end{cases}$$

The Cauchy-Green deformation tensor \mathbf{C} is defined as $\mathbf{C} = \mathbf{F}^T \mathbf{F}$, and $F_{ij} = \frac{\partial \mathbf{x}_i}{\partial \mathbf{X}_j}$ is the deformation gradient tensor. $J_3 = 1$ for incompressible materials.

The N-H model is the idealization of an elastic material typically under small strain conditions. It can be considered as a simplified version of the M-R model. The strain energy function for the N-H model takes the form as follows:

$$W^{\text{NH}} = \frac{\mu}{2}(J_1 - 3) + \frac{\kappa}{2}(J_3 - 1)^2, \quad (8)$$

where μ is the material parameter, κ is the bulk modulus, and J_1 and J_3 are invariants related to the deformation gradient \mathbf{F} . The third model employed is the K-V model, considering the cell membrane as a linear viscoelastic material, in which

$$\boldsymbol{\sigma} = 2\eta \frac{d\boldsymbol{\varepsilon}}{dt}, \quad (9)$$

where η is the viscosity of the membrane, and is set to be 0.02 Pa·s. $\boldsymbol{\varepsilon}$ is the strain of the membrane, and can be calculated by

$$\boldsymbol{\varepsilon}(t) = \frac{\boldsymbol{\sigma}_0}{G}(1 - e^{-t/\tau}). \quad (10)$$

Thus, the stress $\boldsymbol{\sigma}_0$ can be obtained. G and τ are the shear modulus and relaxation time, and are defined as

$$G = \frac{E}{2(1 + \nu)}, \quad \tau = \frac{\eta}{G}, \quad (11)$$

where E is the elastic modulus, and ν is Poisson's ratio.

In the simulations, cells are assumed to be incompressible materials. Therefore, for the M-R and N-H hyperelastic constitutive models, $\nu = 0.5$. However, for the K-V model, since the material exhibits viscoelastic behavior, Poisson's ratio is no longer a constant but varies with time, and the initial Poisson's ratio cannot be set to 0.5^[62]. It is set to be 0.45 in this study.

2.3 Dataset

After determining the constitutive equation for the cell, the finite element method is utilized to simulate the flow-induced deformation of the cell as it passes through a contactless micro-constriction. The grid independence verification has been performed and provided in Appendix S2 in the electronic supplementary material (see <https://doi.org/10.1007/s10483-024-3187-6>). Subsequently, finite element simulations of cell deformation are conducted with 246 different constitutive parameter sets. Among these, there are 85 sets of M-R constitutive equations, 79 sets of N-H constitutive equations, and 82 sets of K-V constitutive equations. For the N-H and K-V models, the constitutive parameters directly determine the elastic modulus E . For the M-R model, E is indirectly set by adjusting the material constants c_1 and c_2 as $E = 6 \times (c_1 + c_2)$ ^[59–61]. Furthermore, in the case of red blood cells, the values of c_1 and c_2 in the M-R model are constrained to satisfy $c_2/c_1 = 0.1$ ^[63]. The experimentally measured range of E for cells via AFM spans from 10^2 Pa to 10^5 Pa^[64]. In our numerical simulations, E is sampled across a range specified as 2×10^2 Pa to 4×10^4 Pa.

After obtaining the cell deformation in the micro-constriction channel, the snapshots of cell deformations are extracted at different time moments, incorporating the information on cell deformation, their corresponding time information, and the horizontal position information. In this study, we define the number of snapshots of cell movement in the microchannel as a parameter n_s , and it is chosen to be $n_s = 1, 6, 11, 16, 21, 26$, and 31. $n_s = 1$ corresponds to considering only static data on cell deformation^[46–47], and the snapshot is extracted near the outlet, referred to as the region of interest as shown in Fig. 1. For other snapshot indices, the selected cell position snapshots capture the cells' locations from their initial positions to the outlet of the computational region. Additionally, the time intervals between these snapshots are not necessarily uniformly distributed. Figure 1 illustrates the selection of n_s ($= 10$) cell snapshots in a micro-constriction channel.

3 ML model

3.1 Characterization of deformable cells

An MI-CNN architecture is developed to predict the elastic modulus E and constitutive equation of cells in the present study. In contrast to the literature available^[44–45,47], the images of cell deformation are not directly utilized as the input of the NN. Instead, the images are pre-processed using the computer vision library OpenCV before training, as shown in Fig. 2. First, the original cell images from numerical simulations (see Fig. 2(a)) are binarized, resulting in the binary images shown in Fig. 2(b). Then, the boundary following algorithm proposed by Suzuki^[65] is used to detect the cell contour in the binary image, and the centroid of this contour is calculated (see the red dot in Fig. 2(c)). Finally, starting from the rear (Point 'A') of the cell, the vectors from the centroid pointing to the contour are obtained sequentially in a counterclockwise direction. These vectors represent the coordinates (x_i, y_i) of the contour points (see Fig. 2(d)). Then, the x_i and y_i coordinates of the contour points are connected in a serpentine manner (see Fig. 2(e)). For a cell with n_c contour points and n_s snapshots, the dataset is represented by a 3D array of size $(2n_s, 2, n_c/2)$, serving as inputs for the MI-CNN. In the present study, it is chosen as $n_c = 80$.

3.2 ML model's architectures

The CNN is a type of NN composed of convolutional layers, each containing multiple filters. In a typical CNN model, the combination of convolutional and pooling layers gradually diminishes the size of the input data, ultimately flattening it into a single-column vector for output prediction (classification or regression) by a fully connected neural network (FNN). Filters are a critical core for feature extraction during the training process, and are continuously adjusted through learning and optimization. These filters slide entirely along the data, generating convolutional features, where the output is the product of the filter weights and elements of each

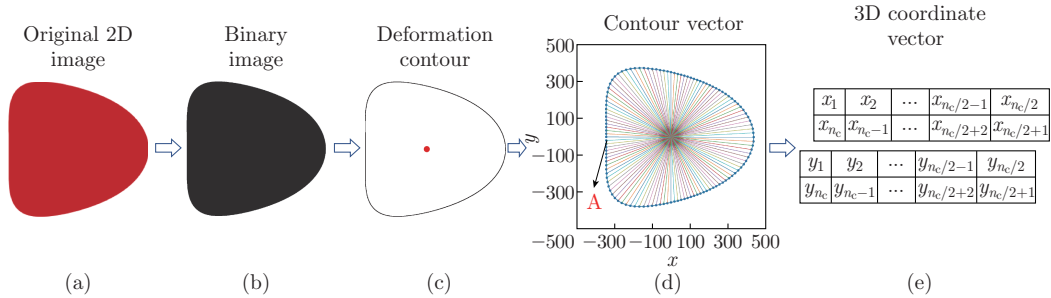


Fig. 2 Procedure for characterizing deformed cell images through OpenCV. The binarization of the original 2D cell deformation image (a) obtained from the numerical calculations results in (b). Subsequently, the cell contour is extracted, and its centroid is computed, yielding (c). Shifting the centroid to the origin and starting from Point “A” (d), the contour points are systematically selected in a counterclockwise manner with an angular interval. All these contour points are connected to the origin, forming a vector. (e) The x_i and y_i coordinates of the contour points are connected in a serpentine fashion, serving as the input of the NN (color online)

small region of the data. Max-pooling is a commonly used pooling operation in the CNN, simplifying the complexity of preserving the maximum value in the pooling kernel through sequential steps. Through the convolution and pooling processes, the dimensions of the input data are significantly reduced while still retaining objects and most important features. CNN demonstrates substantial advantages in handling complex data training tasks. The subsequent step involves flattening the convolutional features into a single-column feature vector, which is then connected to an FNN for the final output result.

The architecture of the MI-CNN model we developed is shown in Fig. 3. This model integrates multi-inputs, including the time information T_i and position information X_i of cell movements into its first fully connected layer, while the time series of cell contours are taken as the input of the convolutional layer to characterize their deformation features. Hence, it is referred to the MI-CNN model. The MI-CNN model incorporates a sequence of 2D convolutional layers and max-pooling layers for effective feature extraction. All the extracted features are flattened and combined with the time information T_i and position information X_i ($i = 1, 2, \dots, n_s$) as inputs for the fully connected layers. Subsequently, after passing through multiple fully connected layers, the regression prediction for the elastic modulus E and classification of the constitutive equation are performed. For the regression problem of the elastic modulus E , the mean absolute error loss function is employed, aiming at minimizing the average absolute error between the predicted elastic modulus and the numerical simulation’s elastic modulus during the training process. For the classification problem of the constitutive equation, the cross-entropy is utilized as the loss function, which is a widely used loss function for multi-class classification problems. The detailed information about the setup of the MI-CNN model for $n_s = 11$ is provided in Table 1.

Besides the MI-CNN model, the conventional CNN model and FNN model without time information T_i and position information X_i of the cells are also considered for comparison in our study. The details of their architectures are provided in Appendixes S3 and S4 in the electronic supplementary material (see <https://doi.org/10.1007/s10483-024-3187-6>).

4 Results

4.1 Regression problem—prediction of cell elastic modulus

To ensure the convergence during a single training process, the ensemble method involving three NN models is used to achieve improved prediction performance compared to individual

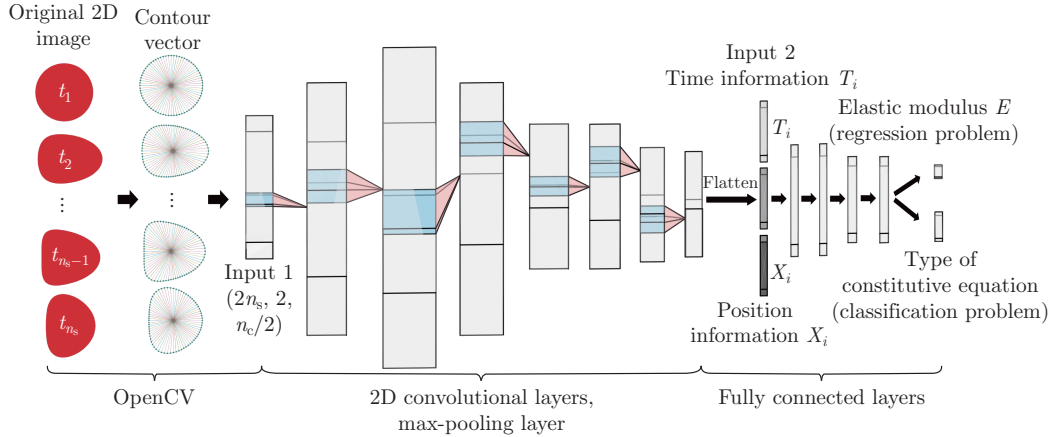


Fig. 3 Architecture of the MI-CNN model. The input of the MI-CNN model is the contour data obtained by processing the deformation images of cells at time steps obtained in the finite element simulation shown in Fig. 2 (Input 1). This model includes a series of 2D convolutional layers for feature extraction and a max-pooling layer. Then, a flat layer is used to place all extracted features into a single-column feature vector. Combined with time and position information, it forms the input for a fully connected layer (Input 2). According to different settings of the loss function, it can be used to predict the elastic modulus E of cells (regression problem) and the type of constitutive equation (classification problem) (color online)

Table 1 Overview of network setups in the MI-CNN model ($n_s = 11$)

Layer	Output size	Activate function	Layer	Output size	Activate function
Input layer 1	(22, 2, 90)	–	Max-pooling layer 1	(5, 2)	–
Convolutional layer 1	(44, 4, 45)	Relu	Input layer 2	$2n_s$	–
Convolutional layer 2	(88, 4, 44)	Relu	Dense layer 1	$10+2n_s$	Relu
Convolutional layer 3	(88, 8, 22)	Relu	Dense layer 2	10	Relu
Convolutional layer 4	(44, 8, 11)	Relu	Dense layer 3	10	Relu
Convolutional layer 5	(22, 8, 10)	Relu	Dense layer 4	10	Relu
Convolutional layer 6	(11, 4, 5)	Relu	Dense layer 5	5	Relu
Convolutional layer 7	(5, 4, 4)	Relu	Output layer	1	–

CNN models^[66]. In the present study, three identical NN architectures are chosen, and the schematic diagram of the model can be found in Appendix S5 in the electronic supplementary material (see <https://doi.org/10.1007/s10483-024-3187-6>). The ensemble method averages the predictions of multiple models, reducing variance and enhancing model performance. The number of models to be trained and combined is a hyperparameter, and it is optimized to be three in our case. The ensemble method is applied separately to the MI-CNN, CNN, and FNN models for training with different numbers of snapshots n_s .

The training results of the MI-CNN model for $n_s = 21$ are shown in Fig. 4. Figure 4(a) presents the training and validation loss histories of the MI-CNN model. Both the training and validation losses converge at the order of 10^{-4} . The coefficient of determination R^2 is utilized to assess the performance of our model, which is given by

$$R^2 = 1 - \frac{\sum_{i=1}^m (E_i - \hat{E}_i)^2}{\sum_{i=1}^m (E_i - \bar{E}_i)^2}, \quad (12)$$

where E_i and \hat{E}_i represent the true elastic modulus E and the predicted elastic modulus for

the i th sample, respectively. \bar{E}_i represents the mean value of the true elastic modulus, and m is the total number of test samples. R^2 ranges from 0 to 1, with higher values indicating better performance. Figure 4(b) illustrates the R^2 plot of the model, and the average R^2 for the training, validation, and test sets are 0.9994, 0.9994, and 0.9996, respectively. This outcome suggests that our MI-CNN model can effectively predict the elastic modulus E of cells based on the deformation cell contour data at 21 time points and their corresponding positions and time information. The root mean square errors (R_{RMSE}) and R_{MAPE} for E are defined as

$$R_{\text{RMSE}} = \sqrt{\frac{1}{m} \sum_{i=1}^m (E_i - \hat{E}_i)^2}, \quad (13)$$

$$R_{\text{MAPE}} = \frac{1}{m} \sum_{i=1}^m |(E_i - \hat{E}_i)/E_i|. \quad (14)$$

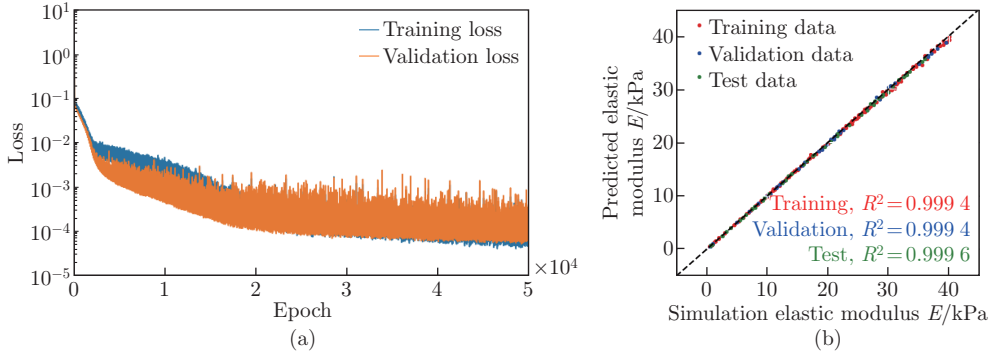


Fig. 4 Prediction of the MI-CNN model on E when $n_s = 21$: (a) training and validation loss history plot after 50 000 training steps and (b) R^2 plot assessing the model's fitting performance to the dataset. The horizontal axis represents the E used in numerical simulations, while the vertical axis represents the NN-predicted E . Points closer to the dashed line indicate better performance. Red, blue, and green dots correspond to training, validation, and test data, with average R^2 of 0.9994, 0.9994, and 0.9996, respectively (color online)

The corresponding R_{RMSE} and R_{MAPE} for this model are 0.2178 and 1.0886%, respectively. These scores perform better than previous 3D-CNNs based on the cell vertex coordinates, which has $R_{\text{RMSE}} = 1.72^{[47]}$ and the MLP network at a single time point with $R_{\text{MAPE}} = 4.2\%^{[46]}$. These results indicate that the present model achieves a high level of accuracy. A comprehensive comparison of model precision reported by fellow researchers is presented in Table 2.

Figure 5 analyzes the influence of n_s on the performance of the MI-CNN, CNN, and FNN models, in which the variations of average R^2 (see Fig. 5(a)), R_{RMSE} (see Fig. 5(b)), and R_{MAPE} (see Fig. 5(c)) for the test sets are plotted with different numbers of snapshots n_s for the three models. Overall, the minimum R^2 reaches 0.9975, and the maximum R_{RMSE} and R_{MAPE} are 0.55 and 6.16%, indicating that these models can effectively predict the elastic modulus of cells. Generally, the R^2 of the MI-CNN and CNN models increase with n_s , while the RMES error decreases with n_s . This suggests that incorporating multiple temporal deformation features into the input contributes to improved accuracy and generalization ability. Moreover, the R_{RMSE} and R_{MAPE} of the MI-CNN model consistently outperform those of the CNN model, indicating that incorporating time and position information into the fully connected layers of the CNN model enhances the model's performance. The FNN model at $n_s = 1$ with a smaller parameter count, similar to the model used by Guo et al.^[46], exhibits a decent ability in accuracy and

Table 2 Comparison of model accuracy with literatures

Model	Input	Target parameter	R^2	R_{RMSE}	$R_{MAPE}/\%$	Ref.
MI-CNN	Time-series ($n_s = 21$) cell contour coordinates	E	0.9996	0.2178	1.0886	Present
MLP	1D capsule contour coordinates	Ca^{G_s}, Ca^{K_s}	—	—	4.2, 7.6	[46]
DCNN	2D capsule images	Shear elasticity G_s , pre-inflation ratio α	—	—	2.6, 4.5	[44]
DCNN-LSTM	Time-series 2D vesicle images	Shear elasticity G_s , membrane viscosity η	—	—	3.65, 3.42	[45]
2D-CNN	2D capsule images	Stiffness K	0.90	3.48	—	[47]
3D-CNN	3D surface coordinate points	Stiffness K	0.98	1.72	—	[47]

generalization. However, it is still inferior to the MI-CNN model in accuracy, and increasing n_s (e.g., $n_s = 26$) can further enhance its performance.

To evaluate the requirement of computational resources as n_s increases, Fig. 5(d) presents the variation in parameter count for the three models with respect to n_s . A smaller parameter count usually implies the need for fewer computational resources during inference (prediction). This is particularly advantageous for running models in resource-constrained environments such as mobile devices or embedded systems. It is found that utilizing the CNN model can significantly reduce the parameter count, and this reduction becomes more pronounced for large n_s .

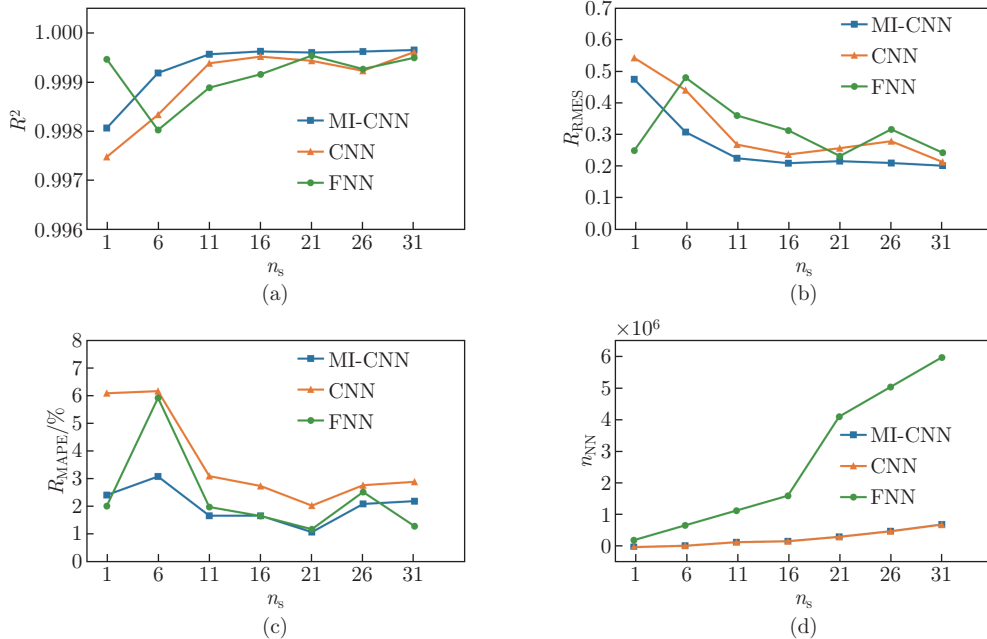


Fig. 5 Effects of n_s on the MI-CNN, CNN, and FNN models: (a) R^2 , (b) R_{RMSE} , (c) R_{MAPE} , (d) the number of NN parameters n_{NN} (color online)

4.2 Classification problem—classification of cellular constitutive equations

In this section, we attempt to classify the constitutive equations of cells using the constructed MI-CNN model. First, a three-class classification is conducted with the datasets of the M-R, K-V, and N-H constitutive models, where $c_2/c_1 = 0.1$ as required for red blood cells according to experimental evidence^[63]. The results indicate that the model can effectively distinguish the K-V model, but fails to accurately classify the N-H and M-R models (see Fig. 6(a)). This

is primarily because if the material constant c_2 of the M-R model is set to zero, the model reduces to the N-H model, i.e., the N-H model can be considered as a simplified form of the two-parameter M-R model. Therefore, due to the parameter setting of $c_2/c_1 = 0.1$ in the M-R model, the influence of the $c_2(J_2 - 3)$ term on the overall mechanical response can be ignored. This point can be further validated by our numerical simulation results. As shown in Fig. 6(b), under the conditions of $E = 2\text{kPa}$ and $T = 11\text{ ms}$, the cell contours obtained from the M-R and N-H models show almost no significant differences.

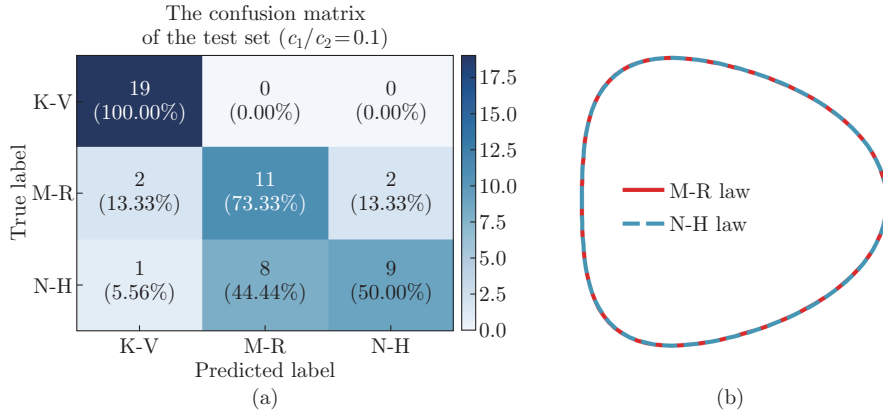


Fig. 6 (a) Three-class classification results of the MI-CNN model ($n_s = 16$) for the K-V, N-H, and M-R constitutive models with $c_2/c_1 = 0.1$. (b) Comparison of cell deformations obtained using the M-R and N-H constitutive equations at an elastic modulus of $E = 2\text{kPa}$ in the microchannel at $T = 11\text{ ms}$ (color online)

To demonstrate the effectiveness of the present model in distinguishing among the different constitution laws, we try to enhance the distinction between the M-R and N-H models by calculating the deformation data for 80 sets of M-R models with $c_2/c_1 = 1.0$, then conduct a three-class classification training. The related results are shown in Fig. 7(a), where the confusion matrix of the test set indicates that the model effectively implements the classification task, achieving an accuracy of 93.88%. This result validates our previous analysis, and demonstrates the effectiveness of this method in distinguishing among different models. Moreover, the regression analysis is performed on the elastic modulus using the M-R dataset with $c_2/c_1 = 1.0$ (see Fig. 7(b)). The results are consistent with the analysis in Subsection 4.1, demonstrating the model's ability in accurately predicting the elastic modulus.

4.3 Influence of noise

Although the images of deformed cells extracted through numerical simulations might exhibit features such as noise-free and high resolution, images or videos obtained in experiments usually contain a significant amount of noise, and have limited resolution. To demonstrate the robustness of the present model, random noise is introduced into the contours obtained from numerical solutions to simulate the experimental data. Three levels of noise models, i.e., small noise, medium noise, and large noise are considered, corresponding to 0.2%, 0.6%, and 1.0% disturbances of the original signals, respectively.

The MI-CNN model with $n_s = 26$ is trained using datasets that incorporate the three levels of noise. The regression results for the elastic modulus E are presented in the form of R^2 plots in Fig. 8. The average R^2 for the test set with small, medium, and large noise are 0.9991, 0.9989, and 0.9963, respectively. These results indicate that the MI-CNN model can effectively predict the elastic modulus of cells based on the deformation data of cell contours at 26 time points, along with their corresponding positional and temporal information. The model demonstrates good applicability and robustness in handling a noisy database.

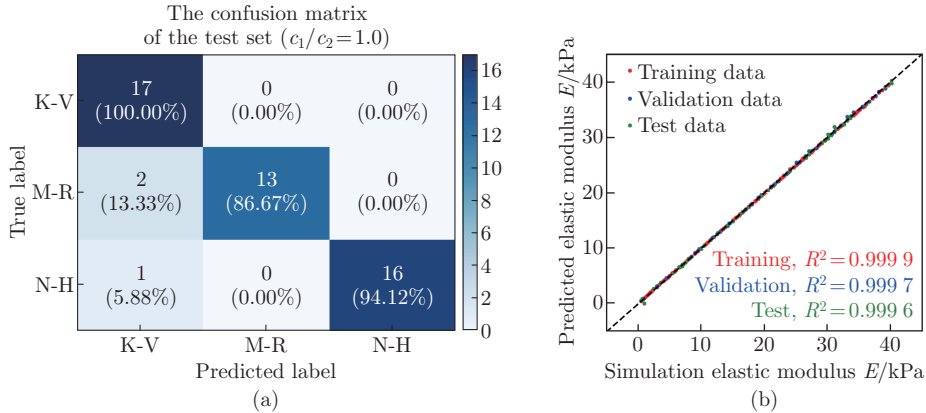


Fig. 7 Results of classification and regression using the K-V, N-H, and M-R constitutive model datasets with $c_2/c_1 = 1.0$: (a) classification results of the three constitutive models using the MI-CNN model ($n_s = 16$), (b) prediction results of E using the MI-CNN model ($n_s = 21$) (color online)

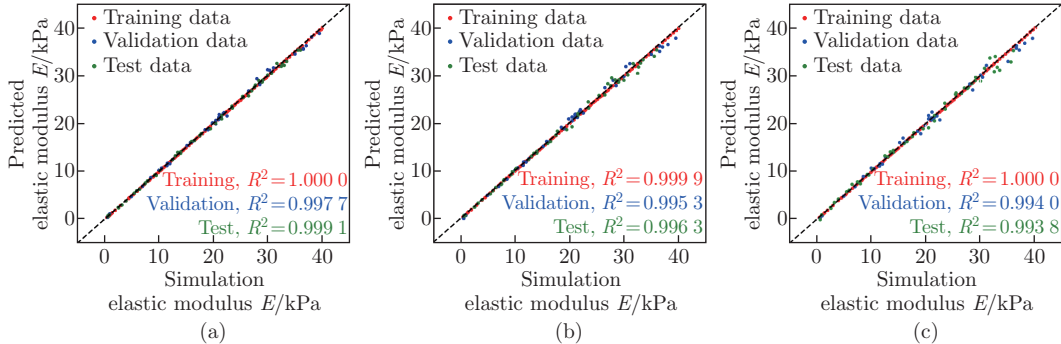


Fig. 8 E regression analysis using the MI-CNN model with $n_s = 26$ on datasets with different levels of noise: (a) small noise, (b) medium noise, and (c) large noise (color online)

Analyzing the results of the validation and test sets for different elastic moduli in Fig. 8, it is observed that the addition of the noise primarily leads to a decrease in the prediction accuracy for cells with large elastic modulus (small deformation), while having little influence on the prediction of cells with small elastic modulus (large deformation). This phenomenon can be ascribed to the fact that when the elastic modulus is large, the deformation of the cell is relatively small, making the cell's deformation highly sensitive to the measurement accuracy. As shown in Fig. 9(a), the variation of the cell roundness D_C with the elastic modulus is depicted based on the deformation of cells in the region of interest. The cell roundness D_C is defined as $D_C = 4\pi A^2/l^2$, where A is the area, and l is the perimeter. When the elastic modulus of the cell is less than 5 kPa, the cell's deformation exhibits extremely high sensitivity to the external force, and even a slight change may cause significant deformation differences in the elastic modulus. However, as E exceeds 5 kPa, the sensitivity to the elastic modulus change gradually decreases. When E exceeds 20 kPa, the cell deformation and elastic modulus become much less correlated under the fluid shear stress in this study. Even with substantial increases in the elastic modulus, the cell's deformation response remains relatively small (see Fig. 9(b)). Although this enhances the difficulty in prediction, the present model still maintains satisfactory performance in prediction accuracy. The R_{RMSE} and R_{MAPE} are 0.331 and 2.240% for small noise, 0.658 and 3.138% for medium noise, and 0.852 and 7.069% for large noise.

The influence of n_s on the performance of the MI-CNN model is analyzed. The model performance is evaluated by R^2 , R_{RMSE} , and R_{MAPE} (see Fig. 10). Overall, the coefficient

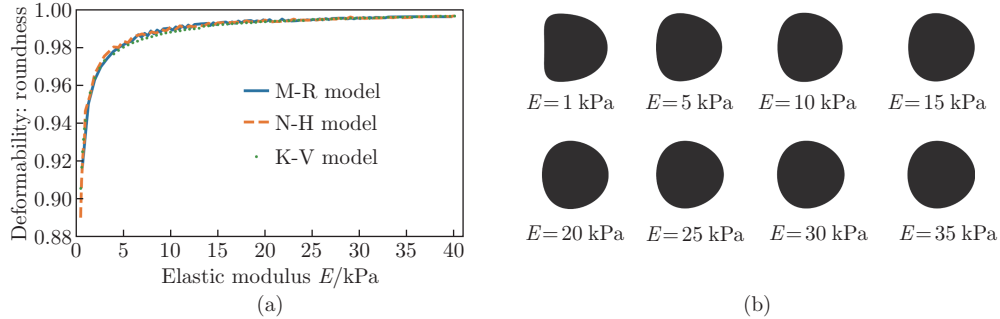


Fig. 9 Influence of elastic modulus E on the deformation ability of cells: (a) the roundness D_C of cells in the region of interest and (b) the deformed cell images in the region of interest for different E (color online)

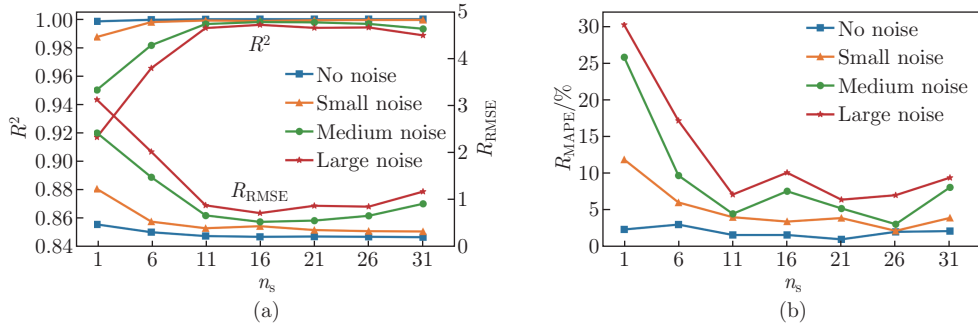


Fig. 10 Influence of n_s on the performance of the MI-CNN model under three levels of noise: (a) R^2 and R_{RMSE} ; (b) R_{MAPE} (color online)

of determination R^2 increased gradually with the growing parameter n_s , corresponding to a gradual decrease in the R_{RMSE} and R_{MAPE} . As the noise level increases, the phenomenon of the RMSE and MAPE decrease while n_s increases becomes more pronounced, especially for smaller n_s (e.g., $n_s = 1, 6$). Two turning points, $n_s = 11$ and $n_s = 26$, are identified. Between these points, the model consistently demonstrates convergent and high-precision predictive results. R^2 can also reach 0.99, indicating that the MI-CNN model could effectively regress the elastic modulus even when noise is included in the data. These results once again validate that incorporating deformation features from multiple time points into the input enhances accuracy and generalization.

5 Conclusions

An NN architecture is proposed to predict the elastic modulus of biological cells in the present study. The training dataset is generated through numerical simulations of cell translocation through a microchannel, and the M-R, N-H, and K-V models are adopted for the cell membrane. An MI-CNN prediction algorithm is developed based on the temporal sequence of cell contours and spatiotemporal information. The results indicate that considering deformation features at multiple time snapshots can enhance the algorithm's accuracy and generalization. Incorporating time and position information in the fully connected layer will improve the algorithm's performance with a minimal increase in parameters. To simulate experimental scenarios, three levels of random noise are introduced to mimic the experimental data. With the presence of noise, the MI-CNN algorithm still provides high-precision prediction of cell elastic modulus, indicating its robustness in handling the problem in reality. Since the MI-CNN algorithm operates on convolutional operations of cell contours at multiple snapshots, it significantly reduces the computational consumption in training. Compared to related publications available, the

advantage of the present algorithm not only lies in its simplicity and robustness, but also in its significant ability in effectively classifying different constitutive models we utilized. Thus, the current framework is promising for the application in high-throughput single-cell characterization on mechanical properties. For this purpose, we are endeavoring to implement experimental measurements to test the effectiveness of the present ML framework. Overall, this study is helpful for future medical and biological applications, such as cancer metastasis monitoring, vascular disease assessment, and analyses of cell health states.

Conflict of interest Guohui HU is an editorial board member for *Applied Mathematics and Mechanics (English Edition)* and was not involved in the editorial review or the decision to publish this article. The authors declare no conflict of interest.

Open access This article is licensed under a Creative Commons Attribution 4.0 International License, which permits use, sharing, adaptation, distribution and reproduction in any medium or format, as long as you give appropriate credit to the original author(s) and the source, provide a link to the Creative Commons licence, and indicate if changes were made. To view a copy of this licence, visit <http://creativecommons.org/licenses/by/4.0/>.

Acknowledgement Beijing Beilong Supercloud Computing Co., Ltd. provides support in computational resources.

References

- [1] EL-ALI, J., SORGER, P. K., and JENSEN, K. F. Cells on chips. *nature*, **442**(7101), 403–411 (2006)
- [2] FRITSCH, A., HÖCKEL, M., KIESSLING, T., NNETU, K. D., WETZEL, F., ZINK, M., and KÄS, J. A. Are biomechanical changes necessary for tumour progression? *Nature Physics*, **6**(10), 730–732 (2010)
- [3] BYUN, S., SON, S., AMODEI, D., CERMAK, N., SHAW, J., KANG, J. H., and MANALIS, S. R. Characterizing deformability and surface friction of cancer cells. *Proceedings of the National Academy of Sciences*, **110**(19), 7580–7585 (2013)
- [4] ISERMANN, P. and LAMMERDING, J. Nuclear mechanics and mechanotransduction in health and disease. *Current Biology*, **23**(24), R1113–R1121 (2013)
- [5] DI CARLO, D. A mechanical biomarker of cell state in medicine. *Journal of Laboratory Automation*, **17**(1), 32–42 (2012)
- [6] GUZNICZAK, E., MOHAMMAD-ZADEH, M., DEMPSEY, F., JIMENEZ, M., BOCK, H., WHYTE, G., and BRIDLE, H. High-throughput assessment of mechanical properties of stem cell derived red blood cells, toward cellular downstream processing. *Scientific Reports*, **7**(1), 14457 (2017)
- [7] GUCK, J. and CHILVERS, E. R. Mechanics meets medicine. *Science Translational Medicine*, **5**(212), 212fs41 (2013)
- [8] TREPAT, X., DENG, L., AN, S. S., NAVAJAS, D., TSCHUMPERLIN, D. J., GERTHOFFER, W. T., and FREDBERG, J. J. Universal physical responses to stretch in the living cell. *nature*, **447**(7144), 592–595 (2007)
- [9] DENG, L., TREPAT, X., BUTLER, J. P., MILLET, E., MORGAN, K. G., WEITZ, D. A., and FREDBERG, J. J. Fast and slow dynamics of the cytoskeleton. *Nature Materials*, **5**(8), 636–640 (2006)
- [10] EKPENYONG, A. E., WHYTE, G., CHALUT, K., PAGLIARA, S., LAUTENSCHLÄGER, F., FIDDLER, C., and GUCK, J. Viscoelastic properties of differentiating blood cells are fate-and function-dependent. *PLoS ONE*, **7**(9), e45237 (2012)
- [11] LAUTENSCHLÄGER, F., PASCHKE, S., SCHINKINGER, S., BRUEL, A., BEIL, M., and GUCK, J. The regulatory role of cell mechanics for migration of differentiating myeloid cells. *Proceedings of the National Academy of Sciences*, **106**(37), 15696–15701 (2009)

- [12] TSE, H. T., GOSSETT, D. R., MOON, Y. S., MASAELI, M., SOHSMAN, M., YING, Y., and DI CARLO, D. Quantitative diagnosis of malignant pleural effusions by single-cell mechanophenotyping. *Science Translational Medicine*, **5**(212), 212ra163 (2013)
- [13] SHAREI, A., ZOLDAN, J., ADAMO, A., SIM, W. Y., CHO, N., JACKSON, E., and JENSEN, K. F. A vector-free microfluidic platform for intracellular delivery. *Proceedings of the National Academy of Sciences*, **110**(6), 2082–2087 (2013)
- [14] LEE, J., SHAREI, A., SIM, W. Y., ADAMO, A., LANGER, R., JENSEN, K. F., and BAWENDI, M. G. Nonendocytic delivery of functional engineered nanoparticles into the cytoplasm of live cells using a novel, high-throughput microfluidic device. *Nano Letters*, **12**(12), 6322–6327 (2012)
- [15] CHAI, J. and SONG, Q. Multiple-protein detections of single-cells reveal cell-cell heterogeneity in human cells. *IEEE Transactions on Biomedical Engineering*, **62**(1), 30–38 (2014)
- [16] UNAL, M., ALAPAN, Y., JIA, H., VARGA, A. G., ANGELINO, K., ASLAN, M., and GURKAN, U. A. Micro and nano-scale technologies for cell mechanics. *Nanobiomedicine*, **1**, 1–5 (2014)
- [17] HAO, Y., CHENG, S., TANAKA, Y., HOSOKAWA, Y., YALIKUN, Y., and LI, M. Mechanical properties of single cells: measurement methods and applications. *Biotechnology Advances*, **45**, 107648 (2020)
- [18] WU, P. H., AROUSH, D. R. B., ASNACIOS, A., CHEN, W. C., DOKUKIN, M. E., DOSS, B. L., and WIRTZ, D. A comparison of methods to assess cell mechanical properties. *Nature Methods*, **15**, 491–498 (2018)
- [19] BENTO, D., RODRIGUES, R. O., FAUSTINO, V., PINHO, D., FERNANDES, C. S., PEREIRA, A. I., and LIMA, R. Deformation of red blood cells, air bubbles, and droplets in microfluidic devices: flow visualizations and measurements. *Micromachines*, **9**(4), 151 (2018)
- [20] TOEPFNER, N., HEROLD, C., OTTO, O., ROSENDALH, P., JACOBI, A., KRÄTER, M., STÄCHELE, J., MENSCHNER, L., HERBIG, M., CIUFFREDA, L., FORD-CARTWRIGHT, L., GRZYBEK, M., COSKUN, Ü., REITHUBER, E., GARRISS, G., MELLROTH, P., HENRIQUES-NORMARK, B., TREGAY, N., SUTTORP, M., BORNHAUSER, M., CHILVERS, E. R., BERNER, R., and GUCK, J. Detection of human disease conditions by single-cell morpho-rheological phenotyping of blood. *eLife*, **7**, e29213 (2018)
- [21] XIE, J. and HU, G. H. Computational modelling of membrane gating in capsule translocation through microchannel with variable section. *Microfluidics and Nanofluidics*, **25**(2), 17 (2021)
- [22] ABKARIAN, M., FAIVRE, M., and STONE, H. A. High-speed microfluidic differential manometer for cellular-scale hydrodynamics. *Proceedings of the National Academy of Sciences*, **103**(3), 538–542 (2006)
- [23] BOW, H., PIVKIN, I. V., DIEZ-SILVA, M., GOLDFLESS, S. J., DAO, M., NILES, J. C., and HAN, J. A microfabricated deformability-based flow cytometer with application to malaria. *Lab on a Chip*, **11**(6), 1065–1073 (2011)
- [24] GOSSETT, D. R., TSE, H. T., LEE, S. A., YING, Y., LINDGREN, A. G., YANG, O. O., and DI-CARLO, D. Hydrodynamic stretching of single cells for large population mechanical phenotyping. *Proceedings of the National Academy of Sciences*, **109**(20), 7630–7635 (2012)
- [25] AI, J. F., XIE, J., and HU, G. H. Numerical simulation of red blood cells deformation in microchannel under zero-net-mass-flux jet. *Acta Physica Sinica*, **69**(23), 234701 (2020)
- [26] LIU, X. Y., AI, J. F., XIE, J., and HU, G. H. Numerical study of opposed zero-net-mass-flow jet-induced erythrocyte mechanoporation. *Applied Mathematics and Mechanics (English Edition)*, **43**(11), 1763–1776 (2022) <https://doi.org/10.1007/s10483-022-2931-6>
- [27] MACQUEEN, L. A., BUSCHMANN, M. D., and WERTHEIMER, M. R. Mechanical properties of mammalian cells in suspension measured by electro-deformation. *Journal of Micromechanics and Microengineering*, **20**(6), 065007 (2010)
- [28] BEECH, J. P., HOLM, S. H., ADOLFSSON, K., and TEGENFELDT, J. O. Sorting cells by size, shape and deformability. *Lab on a Chip*, **12**(6), 1048–1051 (2012)
- [29] OTTO, O., ROSENDALH, P., MIETKE, A., GOLFERS, S., HEROLD, C., KLAUE, D., and GUCK, J. Real-time deformability cytometry: on-the-fly cell mechanical phenotyping. *Nature Methods*, **12**(3), 199–202 (2015)

- [30] ROSENDAHL, P., PLAK, K., JACOBI, A., KRAETER, M., TOEPFNER, N., OTTO, O., and GUCK, J. Real-time fluorescence and deformability cytometry. *Nature Methods*, **15**(5), 355–358 (2018)
- [31] MIETKE, A., OTTO, O., GIRARDO, S., ROSENDAHL, P., TAUBENBERGER, A., GOLFERS, S., and FISCHER-FRIEDRICH, E. Extracting cell stiffness from real-time deformability cytometry: theory and experiment. *Biophysical Journal*, **109**(10), 2023–2036 (2015)
- [32] MOKBEL, M., MOKBEL, D., MIETKE, A., TRABER, N., GIRARDO, S., OTTO, O., and ALAND, S. Numerical simulation of real-time deformability cytometry to extract cell mechanical properties. *ACS Biomaterials Science and Engineering*, **3**(11), 2962–2973 (2017)
- [33] SARKER, I. H. Machine learning: algorithms, real-world applications and research directions. *SN Computer Science*, **2**(3), 160 (2021)
- [34] PRALJAK, N., IRAM, S., GOREKE, U., SINGH, G., HILL, A., GURKAN, U. A., and HINCZEWSKI, M. Integrating deep learning with microfluidics for biophysical classification of sickle red blood cells adhered to laminin. *PLoS Computational Biology*, **17**(11), e1008946 (2021)
- [35] HEIDARI, M., LAKSHMIVARAHAN, S., MIRNIAHARIKANDEHEI, S., DANALA, G., MARYADA, S. K. R., LIU, H., and ZHENG, B. Applying a random projection algorithm to optimize machine learning model for breast lesion classification. *IEEE Transactions on Biomedical Engineering*, **68**(9), 2764–2775 (2021)
- [36] TIAN, Y., LIN, W., QU, K., WANG, Z., and ZHU, X. Insights into cell classification based on combination of multiple cellular mechanical phenotypes by using machine learning algorithm. *Journal of the Mechanical Behavior of Biomedical Materials*, **128**, 105097 (2022)
- [37] PHILLIP, J. M., HAN, K. S., CHEN, W. C., WIRTZ, D., and WU, P. H. A robust unsupervised machine-learning method to quantify the morphological heterogeneity of cells and nuclei. *Nature Protocols*, **16**(2), 754–774 (2021)
- [38] SONG, T. H., SANCHEZ, V., EIDALY, H., and RAJPOOT, N. M. Dual-channel active contour model for megakaryocytic cell segmentation in bone marrow trephine histology images. *IEEE Transactions on Biomedical Engineering*, **64**(12), 2913–2923 (2017)
- [39] HERBIG, M., JACOBI, A., WOBUS, M., WEIDNER, H., MIES, A., KRÄTER, M., OTTO, O., THIEDE, C., WEICKERT, M., GÖTZE, K. S., RAUNER, M., HOFBAUER, L. C., BORNHÄUSER, M., GUCK, J., ADER, M., PLATZBECKER, U., and BALAIAN, E. Machine learning assisted real-time deformability cytometry of CD34+ cells allows to identify patients with myelodysplastic syndromes. *Scientific Reports*, **12**(1), 870 (2022)
- [40] ISLAM, S., SHAH, V., GIDDE, S. T. R., HUTAPEA, P., SONG, S. H., PICONE, J., and KIM, A. A machine learning enabled wireless intracranial brain deformation sensing system. *IEEE Transactions on Biomedical Engineering*, **67**(12), 3521–3530 (2020)
- [41] LEE, S., LUKAN, J., BOYKO, T., ZELENOVA, K., MAKLED, B., PARSEY, C., and DE, S. A deep learning model for burn depth classification using ultrasound imaging. *Journal of the Mechanical Behavior of Biomedical Materials*, **125**, 104930 (2022)
- [42] SHEN, S. C. Y., FERNÁNDEZ, M. P., TOZZI, G., and BUEHLER, M. J. Deep learning approach to assess damage mechanics of bone tissue. *Journal of the Mechanical Behavior of Biomedical Materials*, **123**, 104761 (2021)
- [43] KARNIADAKIS, G. E., KEVREKIDIS, I. G., LU, L., PERDIKARIS, P., WANG, S., and YANG, L. Physics-informed machine learning. *Nature Reviews Physics*, **3**(6), 422–440 (2021)
- [44] LIN, T., WANG, Z., LU, R., WANG, W., and SUI, Y. Characterising mechanical properties of flowing microcapsules using a deep convolutional neural network. *Advances in Applied Mathematics and Mechanics*, **14**(1), 79–100 (2022)
- [45] LIN, T., WANG, Z., WANG, W., and SUI, Y. A neural network-based algorithm for high-throughput characterisation of viscoelastic properties of flowing microcapsules. *Soft Matter*, **17**(15), 4027–4039 (2021)
- [46] GUO, Z., LIN, T., JING, D., WANG, W., and SUI, Y. A method for real-time mechanical characterisation of microcapsules. *Biomechanics and Modeling in Mechanobiology*, **22**(4), 1209–1220 (2023)

- [47] NGUYEN, D., TAO, L., YE, H., and LI, Y. Machine learning-based prediction for single-cell mechanics. *Mechanics of Materials*, **180**, 104631 (2023)
- [48] LIANG, L., LIU, M., and SUN, W. A deep learning approach to estimate chemically-treated collagenous tissue nonlinear anisotropic stress-strain responses from microscopy images. *Acta Biomaterialia*, **63**, 227–235 (2017)
- [49] MARTÍNEZ-MARTÍNEZ, F., RUPÉREZ-MORENO, M. J., MARTÍNEZ-SOBER, M., SOLVESS-LLORENS, J. A., LORENTE, D., SERRANO-LÓPEZ, A. J., MARTÍNEZ-SANCHIS, S., MONSERRAT, C., and MARTÍN-GUERRERO, J. D. A finite element-based machine learning approach for modeling the mechanical behavior of the breast tissues under compression in real-time. *Computers in Biology and Medicine*, **90**, 116–124 (2017)
- [50] XIAO, P., HAQUE, E., ZHANG, T., DONG, X. N., HUANG, Y., and WANG, X. Can DXA image-based deep learning model predict the anisotropic elastic behavior of trabecular bone? *Journal of the Mechanical Behavior of Biomedical Materials*, **124**, 104834 (2021)
- [51] WANG, Z., LUO, W., GAO, L., and LI, M. Modeling the bottom-up filling of through silicon vias with different additives. *15th International Conference on Electronic Packaging Technology*, IEEE, Chengdu (2014)
- [52] YANEN, W., SHENGMIN, W., YAN, X. T., YAO, C., and MING, Y. Computer simulation for bone scaffolds on account of fluid-solid coupling model. *2009 International Forum on Computer Science-Technology and Applications*, IEEE, Chongqing (2009)
- [53] LIU, X., GUI, N., WU, H., YANG, X., TU, J., and JIANG, S. Numerical simulation of flow past stationary and oscillating deformable circles with fluid-structure interaction. *Experimental and Computational Multiphase Flow*, **2**, 151–161 (2020)
- [54] KALLIONTZIS, D. Fluid-structure interaction with ALE formulation and skeleton-based structural models. *Journal of Fluids and Structures*, **110**, 103513 (2022)
- [55] FOURNIER, J. B. and BARBETTA, C. Direct calculation from the stress tensor of the lateral surface tension of fluctuating fluid membranes. *Physical Review Letters*, **100**(7), 078103 (2008)
- [56] PENROSE, J. M. T. and STAPLES, C. J. Implicit fluid-structure coupling for simulation of cardiovascular problems. *International Journal for Numerical Methods in Fluids*, **40**(3-4), 467–478 (2002)
- [57] WEI, X., SANG, J., TIAN, C., SUN, L., and LIU, B. Different types of constitutive parameters red blood cell membrane based on machine learning and FEM. *International Journal of Computational Methods*, **20**(3), 2250057 (2023)
- [58] HAN, Y., LIN, H., DING, M., LI, R., and SHI, T. Flow-induced translocation of vesicles through a narrow pore. *Soft Matter*, **15**(16), 3307–3314 (2019)
- [59] POZRIKIDIS, C. *Modeling and Simulation of Capsules and Biological Cells*, Chapman and Hall/CRC, New York (2003)
- [60] SKALAK, R., TOZEREN, A., ZARDA, R. P., and CHIEN, S. Strain energy function of red blood cell membranes. *Biophysical Journal*, **13**(3), 245–264 (1973)
- [61] BERGSTROM, J. S. *Mechanics of Solid Polymers: Theory and Computational Modeling*, William Andrew, New York (2015)
- [62] HOWELL, P., KOZYREFF, G., and OCKENDON, J. *Applied Solid Mechanics*, Cambridge University Press, Cambridge (2009)
- [63] GREEN, A. E. and ADKINS, J. E. *Large Elastic Deformations*, Oxford University Press, Oxford (1970)
- [64] KUZNETSOVA, T. G., STARODUBTSEVA, M. N., YEGORENKOVA, N. I., CHIZHIK, S. A., and ZHDANOV, R. I. Atomic force microscopy probing of cell elasticity. *Micron*, **38**(8), 824–833 (2007)
- [65] SUZUKI, S. Topological structural analysis of digitized binary images by border following. *Computer Vision, Graphics, and Image Processing*, **30**(1), 32–46 (1985)
- [66] DIETTERICH, T. G. Ensemble methods in machine learning. *International Workshop on Multiple Classifier Systems*, Springer, Heidelberg, 1–15 (2000)